New Insights on the Reversible Lithiation Mechanism of TiO$_2$(B) by Operando X-ray Absorption Spectroscopy and X-ray Diffraction Assisted by First-Principles Calculations

Marcus Fehse,*[†] Mouna Ben Yahia,[†,‡] Laure Monconduit,[†,‡] Frédéric Lemoigno,[†,‡] Marie-Liesse Doublet,[†,‡] Florent Fischer,[§] Cécile Tessier,[§] and Lorenzo Stievano*[†,‡]

[†]ICGM CNRS and Université Montpellier 2, Place E. Bataillon, 34095 Montpellier, France
[‡]Réseau sur le Stockage Electrochimique de l'Energie, CNRS FR3459, 80039 Amiens Cedex, France
[§]SAFT, Direction de la Recherche, 111-113 Bd Alfred Daney, 33074 Bordeaux, France

Ⓢ Supporting Information

ABSTRACT: Operando X-ray absorption spectroscopy (XAS) and X-ray diffraction (XRD) measurements provide new insights on the mechanism of lithium insertion into TiO$_2$(B). The investigation of the evolution of electronic, long-range, and local structure during electrochemical cycling indicates a purely monophasic insertion mechanism upon lithium insertion, while global and local structure are only slightly modified. While XRD reflects an anisotropic lattice expansion, EXAFS reveals a wide distribution of Ti−O bond length, in line with the presence of two distinct distorted octahedral Ti environments, in agreement with previous DFT calculations. Upon lithium insertion, these Ti−O coordination shells undergo significant modifications which are enhanced once the insertion of 0.4 Li is exceeded, connoting a two regime process that is in good agreement with the electrochemical signature of this material. DFT calculations and local chemical bond analyses were coupled with experimental results, thus providing additional insights into the structural response of TiO$_2$(B) upon lithiation.
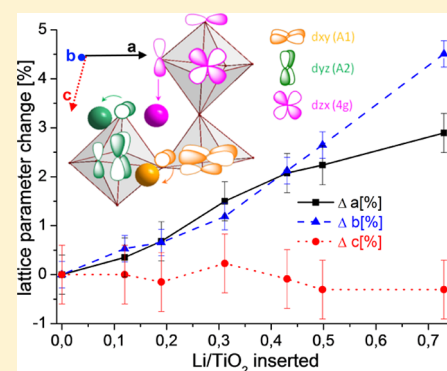
INTRODUCTION

In the search for suitable high power battery negative electrode materials, the bronze phase also known as TiO$_2$(B) is a potential candidate with distinct advantages over other titania-based insertion materials. While its increased theoretical capacity (336 mAh/g), compared to commercialized LTO (Li$_4$Ti$_5$O$_{12}$, Cap$_{theo}$ 175 mAh/g), has been known for quite some time,[1−3] its superior rate capability compared to the largely studied anatase phase has been more recently claimed in various papers.[4−8] These assets, in combination with the intrinsic benefits of titania-based materials, such as environmental benignancy, cost efficiency, long cycle life and high safety due to elevated insertion potential, endow TiO$_2$(B) to be a promising alternative negative electrode material.[9]

Despite the numerous experimental studies showing favorable insertion properties of TiO$_2$(B), there are comparatively few works dedicated to the understanding of the physicochemical foundations of such performances. In a recent publication, we showed that the superior rate capability of TiO$_2$(B) can be attributed to lower internal resistance at increased cycling rate compared to other more common TiO$_2$ polymorphs such as anatase.[8] Other research groups, on the other hand, attribute this superiority to the low density or to the unique open channel structure.[3,10−12] Zukalová et al. were the first to introduce the concept of pseudocapacitive storage for describing the Li$^+$ storage mechanism in TiO$_2$(B).[5] They

describe a faradaic surface storage mechanism which is not restricted by slow solid-state diffusion. Such a mechanism is enabled by the monoclinic C2/m open channel structure which allows not only fast Li$^+$ transport, but also provides easily accessible Li$^+$ insertion sites within the channels.[5,13]

Armstrong et al. studied the Li coordination sites in a partially lithiated sample with average composition Li$_{0.15}$TiO$_2$(B) by neutron diffraction.[14] This sample was found to be a disordered mixture of TiO$_2$(B) and of the partially lithiated phase Li$_{0.25}$TiO$_2$(B), where Li$^+$ occupies only the channel site, C. These data where backed-up by DFT calculations, which also suggested the higher stability of the C sites compared to the other two, A1 and A2, located on the (001) plane and between the oxygen atoms bridging adjacent layers in the (001) plane, respectively. However, they also found that upon further lithiation the C insertion site becomes less and less stable compared to the other two. More recently, the assertion that these C-sites are the energetically preferred lithium insertion ones, has been questioned by the comprehensive computational study of Morgan et al.[6] In the present work, we confirm the study of Morgan et al. by directly correlating the titanium local distortions to the site preference

and to the structural changes expected. It is challenging to answer this question without the support of experimental studies, since various parameters, such as the degree of filling,[14] or the morphology,[15] are claimed to have an effect on the stability of the different insertion sites.

In one of the few experimental studies aiming at elucidating the insertion mechanism of $TiO_2(B)$, and conducted by ex situ XAS, Okumura et al. claim that Li storage in nanostructured $TiO_2(B)$ occurs in the space charge layer (SCL). Therefore, it neither inflicts changes in lattice nor in the electronic structure resembling more to a fully capacitive double layer storage than to a pseudocapacitive faradaic storage.[16] For bulk $TiO_2(B)$, however, they suggest a two regime insertion mechanism with preferred C site filling,[17] in line with the cited results of Armstrong et al.[14] which have been questioned by more recent publications.[6,18,19] In their recently published ex situ NMR study, Hoshina et al. suggest that surface storage in nanoscaled ($\emptyset \approx 100$ nm) $TiO_2(B)$ occurs only up to 0.18 Li.[20] Upon further lithiation, lithium is stored primarily in A2 site. Furthermore, they claim that lithiation exceeding 0.45 Li leads to the filling of A1 site causing a growing local lattice distortion eventually impeding Li diffusion. In our recently published work we demonstrate that by coupling measurement results from operando XRD and XAS a reliable and comprehensive picture of the lithiation and delithiation process of TiO_2 anatase can be obtained.[21]

In this work we present a thorough study by operando XAS and XRD of the insertion of lithium in $TiO_2(B)$. We show insights on the evolution of electronic, local, and lattice structure during lithiation in order to elucidate the physicochemical mechanisms and processes that are the basis for the favorable cycling properties of $TiO_2(B)$. These experimental results are supported by local chemical bond analysis investigated within the conceptual DFT framework to shed light on the debated and still unclear energetics of lithium insertion sites of the $TiO_2(B)$ structure.

■ EXPERIMENTAL SECTION

Synthesis and Electrode Preparation. The TiO_2 samples were synthesized via hydrothermal synthesis, a detailed description has been previously published elsewhere.[8] Briefly, TiO_2 powder was dispersed in an alkaline aqueous solution and kept in an autoclave for 72 h at 150 °C. After cooling to room temperature, the material was treated with HCl for ion exchange and then washed with deionized water upon total removal of chlorides. Finally, the samples were calcined in air at 450 °C.

Self-supported electrodes were obtained by mixing $TiO_2(B)$ with 8% carbon black and 20% PVdF in an acetone based slurry, which was subsequently tape casted with a doctor blade on a smooth clean surface. After air drying, electrodes were cut out and pealed off from the smooth surface.

Methods. Operando X-ray absorption spectroscopy and X-ray diffraction were performed using a customized cell with a sturdy stainless steel body and Beryllium window as both closure and current collector.[22] Self-supported electrode films prepared as described above were mounted in half cell configuration against Li metal using EC:PC:3DMC 1 M $LiPF_6$ and Celgard as the electrolyte and the separator, respectively.

XRD measurements were carried out using a Philips X'pert diffractometer with Cu Kα radiation at room temperature, in the range from 20 to 50° 2 Θ using a step size of 0.05° and

dwell time of 700 s, yielding to the acquisition of about one diffraction pattern per hour. The computer program Powder Cell[23] as well as Fullprof[24] were used to deduce unit cell parameters. Full pattern matching was performed based on crystal structure published by BenYahia et al.[25] to refine the cell parameters a, b, and c, but no atomic position.

XAS measurements were carried out on beamline A 140 (HASYLAB@DESY, Hamburg, Germany) and beamile XAFS (Elettra, Trieste, Italy). Ti K-edge spectra were recorded in the transmission mode in the range 4800−6100 eV, recording about three spectra per hour. Fourier transform were performed using k^2 weighing and the structural parameters were determined by curve-fitting procedures using the IFEFFIT software suite[26] on the basis of the published $TiO_2(B)$ crystal structure by BenYahia et al.[25] We included in the fit one or two two-leg contributions for six nearest oxygen atoms and three two-leg contributions carrying seven nearest Ti atoms. No three-leg contributions were considered. For each two leg contribution, the position (delR) and the Debye−Waller factor (ss) were fitted individually.

Electrochemical cycling was carried out in the galvanostatic mode on a *Biologic* multichannel potentiostat. Measurements were carried out at cycling rate of C/20, where 1C corresponds to the insertion of 1 mol Li per hour into 1 mol TiO_2, and is equivalent to a current of 336 mA/g.

Calculations were performed within the framework of Density Functional Theory (DFT) and its DFT+U variant[27] using the rotationally invariant method of Dudarev[28] as implemented in the Vienna Ab-Initio Simulation Package (VASP).[29,30] The generalized gradient approximation of Perdew, Burke, Ernzerhof (PBE)[31] was chosen for exchange and correlation energy. The valence/core interaction was described in the projected augmented wave formalism (PAW)[32] with Ti(2p) and Li(1s) included in the atomic valence shells. Convergence of the calculations was checked with respect to the energy cutoff (up to 800 eV) and the k-points grid (2 × 6 × 4) leading to reliable converged structures. Atomic coordinates and lattice parameters were fully relaxed using conjugate gradient energy minimization with a force tolerance set to 1.10^{-3} eV/Å.

Fukui functions were also computed for various Li_xTiO_2 compositions. Within the conceptual DFT framework,[33] they are defined as the change in the system electron density due to an added charge (electron or hole):

$$f^{\pm}(r) = \left(\frac{\partial \rho(r)}{\partial N} \right)_v \tag{1}$$

where N is the amount of added charge and v assumes no structural change between the neutral and charged systems. The $f^+(r)$ and $f^-(r)$ quantify the electronic response of the system to the addition of a fraction of electron and hole, respectively and are often used to probe the frontier orbitals of the system, namely the highest occupied (HO) and lowest unoccupied (LU) crystal orbitals. In contrast to spin density map plots, Fukui functions include the polarization effects induced by the change in density on all orbitals (not only the frontier orbitals) and are therefore meaningful descriptors for describing electrochemical properties.

■ RESULTS

The here presented material is composed of $TiO_2(B)$ rich nanorods with average diameter of 40−60 nm and a specific

surface area of 50 m²/g. A comprehensive characterization of this material can be found in our previous publication.[8]

Operando XRD. The evolution of the diffraction pattern of $TiO_2(B)$ upon consecutive Li^+ insertion (charge) and deinsertion (discharge) is presented in Figure 1. The only
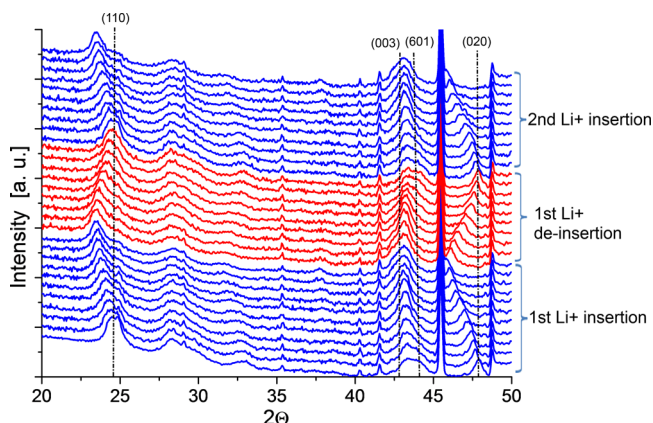

Figure 1. Operando XRD measurement upon consecutive charge (Li^+ insertion) and discharge (Li^+ deinsertion) of $TiO_2(B)$ self-supported film, showing reversible peak shift of (110), (003), (601), and (020), all attributed to $TiO_2(B)$, while peak at 46° results from Be window.

reflection peak that cannot be attributed to $TiO_2(B)$ at 46° corresponds to hexagonal Be originating from the Be window of the in situ cell. This feature can be used to calibrate the diffraction patterns.

A gradual shift of the Bragg peaks of $TiO_2(B)$ is observed upon lithiation, indicative of a single phase transformation, which is shown to be perfectly reversible in lithium deinsertion. The main changes are observed for the (020) and (110) reflection at 48.5° and 24.9°, respectively, the $(60\overline{1})$ at 44.5° undergoes a less pronounced position change.

Because of the low crystallinity of the $TiO_2(B)$ samples and the short acquisition time induced by the operando set up, the obtained diffraction patterns are not suitable for a complete Rietveld refinement. A simple pattern matching could nevertheless be performed by following the shift of the main diffraction peaks $TiO_2(B)$ with the computer program *Powder Cell*, which provided a first estimate of the changes in the lattice parameters with Li content. The evolution of the lattice parameter as a function of the amount of inserted lithium is shown in Figure 2. By accumulating multiple diffraction patterns of the fully lithiated and of the pristine state, we were able to obtain sufficiently good patterns to perform a full pattern matching for these two conditions, using much more performing computer program *FullProf*. The obtained data points are shown as hollow markers in Figure 2, and follow well the trend of those obtained using the computer program *Powder Cell*.

After the reaction of ≥0.7 Li, an increase of the lattice parameters a and b of 2.9 and 4.5% is observed, respectively, while c remains virtually unchanged within the experimental error. This anisotropic expansion agrees well with the findings by Armstrong et al.[14] and with the orbital interpretation given below. Applying the full pattern matching method, the expansion in a and b is somewhat reduced to 1.7 and 3.6%, respectively. The discrepancy between the two evolution methods can be explained by the variation of the angle β, which results in almost 1.5% in the full pattern matching,
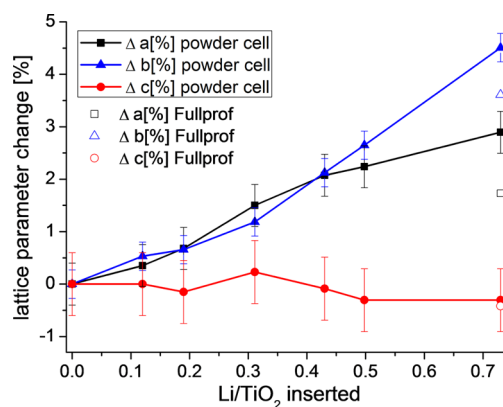

Figure 2. Modification of a, b, and c lattice parameters as a function of the amount of lithium inserted in $TiO_2(B)$ calculated from the evolution of the XRD patterns using *Powder Cell* (filled markers) and full pattern matching with *FullProf* (hollow markers).

whereas the angle could not be varied in the analysis with the computer program *Powder Cell* due to the small number of reflections used for the evaluation of the lattice parameters.

Operando XAS. The modification of the Ti K-edge (4966 eV) upon lithium insertion along with the shift of the Ti K-edge position throughout reduction and subsequent oxidation are presented in Figure 3a and b, respectively. The changes in the pre-edge features are attributed to the filling of Ti 3d orbitals and changes in the Ti-coordination sphere (local symmetry of the TiO_6 octahedra), while the change in position of the K-edge is directly connected to the oxidation state of the emitting Ti atom.[34−37] Upon lithium insertion, Ti^{IV} is reduced to Ti^{III}, which is expressed by a shift of the absorption edge to lower energies. It is noteworthy that this process is largely reversible, although at the end of charge, the starting point of the pristine TiO_2 is not completely recovered. Such irreversibility has been previously reported for TiO_2 based electrodes.[8,35,38−40] Accordingly, it could be an indication of parasitic reactions leading to stable lithium compounds, or of partial lithium trapping in irreversible sites during the first Li^+ insertion, thus, avoiding pure Ti^{IV} recovery at the very end of charge.

The evolution of the EXAFS signal with lithium insertion, and that of the corresponding FT schematically representing the average distribution of the next neighbors to the absorbing Ti-center, are presented in Figure 4a and b, respectively. The black lines resemble the non lithiated state while with growing lithiation the color fades to light gray. For the sake of clearness only four XAFS curves at different stages of lithiation have been selected in Figure 4a. Based on the good quality of the EXAFS data, the FT was performed using a sinusoidal window in the range $2.5 < k < 12.5$. The fitting of the EXAFS spectra in the R range 1.1−3.5 Å was performed considering several combinations for the Ti−O distances comprising the six nearest oxygen neighbors, as well as fitting the following contributions with three Ti−Ti shells. Further information can be found in the Supporting Information.

Concerning the first Ti−O shell, it must be recalled that two different Ti crystallographic sites were identified in the published structure of $TiO_2(B)$.[25] The two octahedral titanium environments, shown in the top of Figure 7, are quite distorted, with a wide distribution of Ti−O distances. One of them features a particularly long Ti−O distance ≥2.3 Å. This site can thus be considered almost as a five-fold square pyramidal coordinated environment named Ti1, which differs significantly
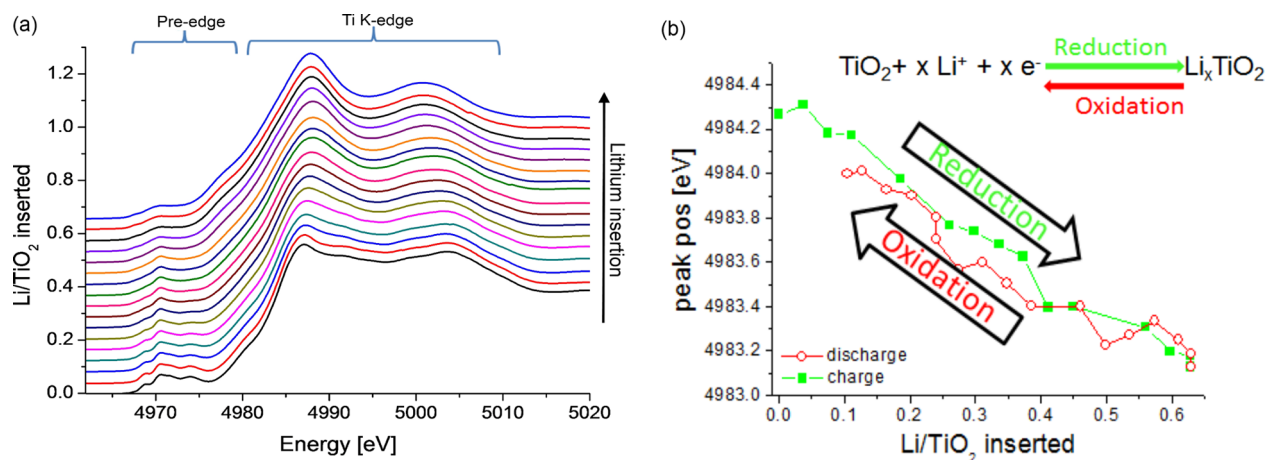
Figure 3. (a) Evolution of Ti K-edge upon Li$^+$ insertion and (b) reversible shift of Ti K-edge position during reduction and subsequent oxidation of TiO$_2$(B) rich sample.

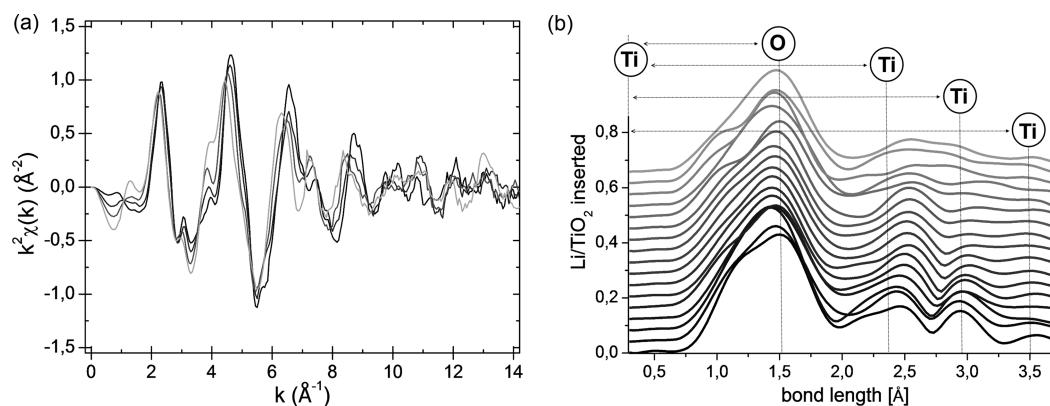**Figure 4.** (a) EXAFS curves at different stages of lithiation and (b) relative phase-uncorrected FT signals of TiO$_2$(B) as a function of inserted lithium. Dotted lines are roughly indicating the position of the contribution of next neighbors of Ti central atom.
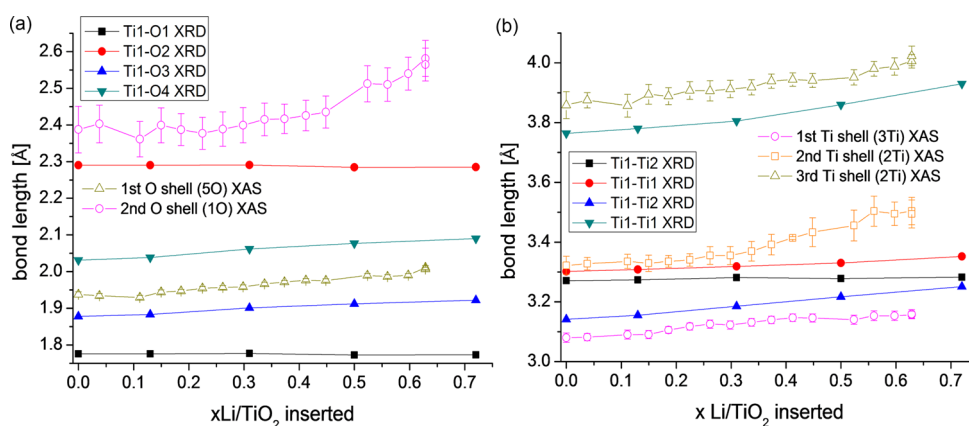

Figure 5. Bond length modification upon lithium insertion derived from FT EXAFS signal and from XRD for (a) Ti−O and (b) Ti−Ti next neighboring shells.

from the less distorted six-fold coordinated Ti2 environment. This large distribution of distances is globally included in the first peak of the FT signal. A single unequivocal fit of this peak by including a different spectral contribution for each possible Ti−O distance is virtually impossible to obtain, due to very strong correlation between the different fit parameters. Therefore, ranged-selected atoms of the same kind are usually grouped in shells, reducing strongly the number of independent fitting parameters, and hence also the possible correlations

between them. An average Ti−O distance is then obtained, and the width of the distribution of distances can be estimated from the value of the Debye−Waller factor.

In this case, we obtained best results (in terms of quality of the fit) for simulating the contribution of the six nearest neighboring oxygen by grouping them in two shells. One presenting five nearest atoms at 1.9 Å and a second close shell containing one oxygen at 2.4 Å (see Supporting Information (SI-Figure 1)). Similarly, the best reproduction of the following

spectral features were obtained using three Ti—Ti shells accounting for a total of seven Ti atoms, in agreement with the crystal structure of $TiO_2(B)$.

From the evolution of average Ti—O distances during electrochemical cycling, we could derive the modification of bond lengths upon lithium insertion, which is plotted in Figure 5 for (a) Ti—O and (b) Ti—Ti distances, respectively. The EXAFS results are compared to chosen bond lengths, derived from operando XRD data. The latter were calculated assuming a simple stretching of the Ti—O and Ti—Ti distances proportional to the observed lattice expansion without structural optimization, and can therefore provide some orientation on the evolution of the average bond distances.

Upon lithium ion insertion, a smooth, gradual expansion of the bond length is found for the inner Ti—O bonds shell of the Ti centers. The plot of the XRD derived bond lengths follows the same slope, which is in line with the idea that the XAS results can be considered as an average distribution of these individual Ti—O bond lengths. For the outer oxygen shell, the XAS and XRD derived bond length goes hand in hand showing that the bond length remains more or less constant up to about 0.4 Li. During this part of the lithiation, therefore, the two Ti—O shell get slightly closer to each other, suggesting that the distribution of the different Ti—O bond lengths becomes somewhat narrower than in the starting material. Once lithium insertion exceeds this value, however, a strong increase of the largest bond length is observed, indicating a strong variation from the octahedral coordination of the Ti centers during this part of the lithiation. Two different structural responses are therefore observed for this system during lithiation with a threshold value of ≈ 0.4 Li in line with the observation of the two peaks found in the derivative of the potential curve at ≈ 1.5 V, forming the characteristic $TiO_2(B)$ twin peak. This point will be addressed in more detail later on.

For the Ti—Ti bonds, which are presented in Figure 5b, the gradual expansion found by EXAFS agrees well with the expansion expected from the XRD data within the error bars. The expansion of bond lengths upon lithium insertion is highly reversible upon lithium deinsertion (not shown), just like the alteration of the crystal lattice. As mentioned above, the evolution of the Debye—Waller factor σ^2, shown in Figure 6, can be seen as a crude estimate of static disorder of the system. Its value for the Ti—O bonds increases somewhat up to 0.2 Li, and then remains almost constant. This observation is in line with the existence of a somewhat larger distribution of Ti—O
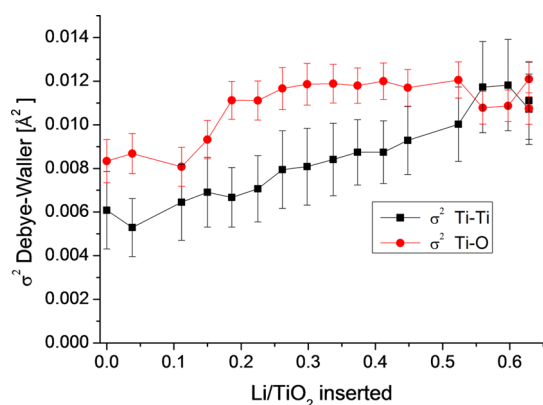
distances when similar amounts of Ti^{III} and Ti^{IV} are present in the system. For the Ti—Ti bonds, a smooth but gradual increase is observed upon lithium insertion. This indicates that Li^+ intercalation inflicts a reduction of the middle-range order of the system, which can also be seen by decreasing intensity and definition of next neighbor contributions (see Figure 4). Upon Li^+ deinsertion (not shown), the initial status is largely retrieved, implying good reversibility.

As mentioned above, despite the appealing properties of $TiO_2(B)$ for application in LIB, few experimental studies focusing on elucidating internal mechanism and processes upon cycling of $TiO_2(B)$ have been published. To the best of our knowledge, the only existing XAS study on lithium insertion in TiO_2 is an ex situ study recently published by Okumura et al.[16,17] However, their results are somewhat contradictory to ours. On the one hand, they show that lithium insertion of up to 0.86 Li has no effect on the XANES or EXAFS spectra for nanosized $TiO_2(B)$ wires ($\varnothing \leq 100$ nm). They attribute the absence of local or electronic structure modification to the fact that in nanosized $TiO_2(B)$, the majority of storage occurs close to the surface within the space charge layer (SCL). This does not rely on faradaic Ti reduction nor inflict structural changes.[17] These results are rather different from our findings for $TiO_2(B)$ samples which have a comparable specific morphology and were obtained using the same synthesis method. The reason for this discrepancy could be related either to the ex situ sample preparation and differences in electrode formulation, or the fact that the observed spot of the sample might not be representative for the general material behavior.

On the other hand, Okumura et al. state significant changes for $TiO_2(B)$ bulk material ($\varnothing \approx 650$ nm) upon lithium insertion. Smooth and gradual expansion of both Ti—O and Ti—Ti bond lengths up to an inflection point at ≈ 0.5 Li were observed, followed by a sudden and significant increase of bond lengths and Debye—Waller factor. On the basis of this observation, they concluded that a two-step Li-insertion mechanism occurs. Based on the mechanism presented by Armstrong et al.,[14] they proposed that lithium is intercalated in $TiO_2(B)$ filling first C and A2 sites, supposedly involving little structural changes, and second of the A1 site, which was said to involve a strong distortion of the Ti coordination. The order of lithium site occupation was attributed on the basis of the mechanism proposed by Arrouvel.[13] As we will demonstrate in the following, such a mechanism which has already been questioned by Morgan et al.[6] and Dalton et al.[18] on the basis of Li-site relative energies, is unlikely.

We believe that the disagreement between Okumura et al. results and our findings arises from the choice of fitting parameters, in combination with the reduced number of data points due to ex situ measurement. In fact, Okumura and co-workers fitted the 6-fold octahedral titanium environment with only one shell, which is inconsistent with the local environment of Ti1 and Ti2 previously reported by Ben Yahia et al.[25] Considering the wide variation of Ti—O bond lengths within the $TiO_2(B)$ structure (see top of Figure 7) and, in particular, taking into account the large increase of one of the bond lengths compared to the other five, a large variation of the Ti—O average distance, and hence, Debye—Waller factor is expected if only one shell is used to fit this peak. By performing fits with different oxygen repartition models, we notice that the quality of the fit is much improved by using two oxygen shells containing five plus one atoms, allowing us to better follow the profile of the closest peak in the FT. See Figure S1 in
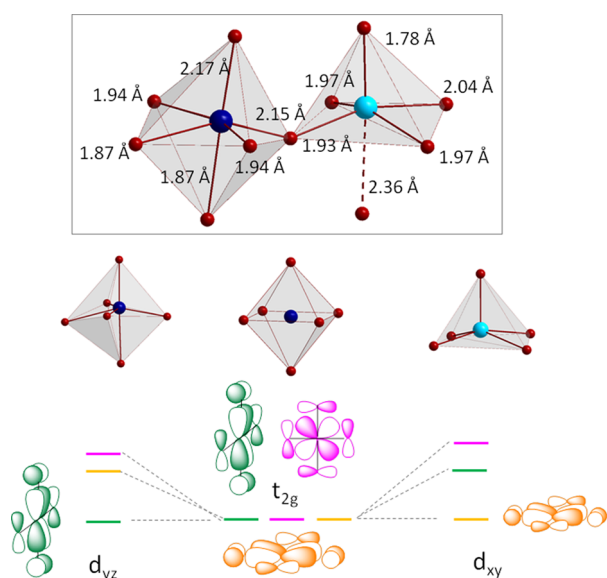

Figure 6. Evolution of Debye—Waller factors of Ti—O and Ti—Ti shells upon lithium insertion.

Figure 7. Top: Ti1 (cyan) and Ti2 (blue) local environments as computed for $TiO_2(B)$. Bottom: Orbital splitting of the t_{2g} orbitals of the regular octahedron (d_{xy}, d_{yz}, and d_{zx}) for the pyramidal and pseudo-octahedral environments of Ti1 and Ti2, respectively.

Supporting Information for comparison of different oxygen repartition models. As a consequence, Okumura et al. observe the above-described distortion beyond the inflection point only indirectly by an abrupt rise in Debye−Waller factor, which confirms the increase in bond lengths distribution range and confirms our choice of using two shells for the fitting of the first peak of the FT signal. Furthermore, they report a strong expansion of the entire TiO_6 octahedra for $x \leq 0.5$ Li. In this aspect their interpretation differs from ours as we show that only the outer oxygen shell changes significantly during the second part of the lithiation (see Figure 5a).

■ DFT CALCULATIONS AND DISCUSSION

In order to validate the previous assumption, DFT calculations were performed on the $Li_xTiO_2(B)$ phases, focusing on low Li contents (up to 0.25) with the aim to establish a direct correlation between the Ti1 and Ti2 local environments and the structural response of the system to the electrochemical reduction. For the sake of comparison with previous works[6,13,18,41] the A1 (4i), A2 (4i′), C (2b), and C′ (2a) sites have all been considered in our calculations. Note that C(0,0.5,0) and C′(0,0,0) sites are related by a shift along the b-axis and are considered not to be occupied simultaneously. This is fully consistent with the intermediate 4g(0,y,0) Wyckoff position generally obtained after full structural relaxation by the different authors, including us. We will hereafter consider only site 4g as the third Li site in the $TiO_2(B)$ structure. Moreover let us recall that the Ti1 and Ti2 coordination spheres are strongly distorted[25] toward a pyramid-like environment for Ti1 (characterized by one short, one long and four medium Ti1−O bonds) and a so-called pseudo-octahedral environment for Ti2 (characterized by two short, two medium and two long Ti2−O bonds). In a molecular orbital (MO) picture, such local distortions are expected to split the t_{2g} MOs of the regular octahedra (i.e., d_{xy}, d_{yz}, and d_{xz}) in such a way that the lowest unoccupied orbitals of the $Ti1^{IV}$ and $Ti2^{IV}$ ions, the electronic levels involved in the electrochemical process at the very

beginning of discharge, are the d_{xy} and d_{yz}, respectively (see bottom of Figure 7).

A simple visualization of the three d_{xy}, d_{yz}, and d_{xz} orbitals on the $TiO_2(B)$ structure (see Figure 8) allows discrimination, which among the A1, A2, and 4g sites is activated by the electrochemical reduction.
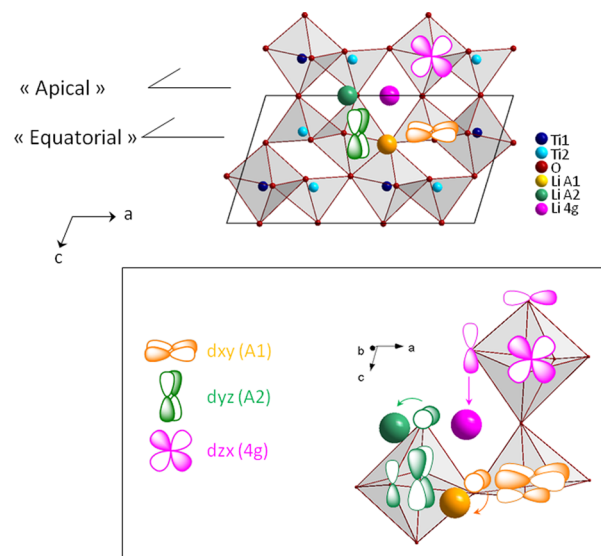

Figure 8. (Top) Superimposition of the d_{xy} (orange), d_{yz} (green), and d_{zx} (pink) orbitals of the TiO_n ($n = 5$ or 6) polyhedra on the unit cell crystal structure of $TiO_2(B)$. As computed for $TiO_2(B)$, where the apical and equatorial planes are identified on the left part of the figure. (Bottom) Illustration of the Ti(d)-O(2p) orbital interactions showing the O−Li site activation.

The d_{xy} expands in the (a,b) plane and make antibonding π-like interactions with the oxygen of the so-called equatorial plane and non bonding interactions with the oxygen of the so-called apical plane. In contrast, the d_{yz} and d_{xz} orbitals expand in the (b,c) and (a,c) planes and make antibonding π-like interactions with the oxygens of both the equatorial and the apical planes. The filling of each of these orbitals should then selectively affect the unit cell parameters of the $TiO_2(B)$ structure and also selectively increase the electron density of oxygens lying either in the equatorial plane (d_{xy}) or in both the equatorial and apical planes (d_{yz} and d_{xz}). Obviously, the increased electron density on selected oxygens will, in turn, selectively promote the A1 (d_{xy}), A2 (d_{yz}), and 4g (d_{xz}) sites, as illustrated on the qualitative scheme of Figure 8. Note that the C site does not correspond to a well-adapted symmetry to interact with the O(2p) orbitals of its first neighboring shell, which explains why it generally moves along the b-axis out of its initial 2b(0,0.5,0) Wyckoff position to reach an intermediate y-coordinate between C and C′. This simple analysis shows that Ti(d)-orbitals can be seen as quantification axes that selectively spot, among the available cationic sites, which one is activated by the electrochemical reduction.

To validate this qualitative approach and extend it to the bulk, the $f^+(r)$ Fukui function of the $TiO_2(B)$ structure was computed within the DFT+U framework, using various U values (U = 0, 4, and 7 eV). As mentioned in Methods, the $f^+(r)$ quantifies the change in the electron density due the addition of a fraction of an electron. In other words, it indicates how the system responds to an electronic reduction and which orbital is
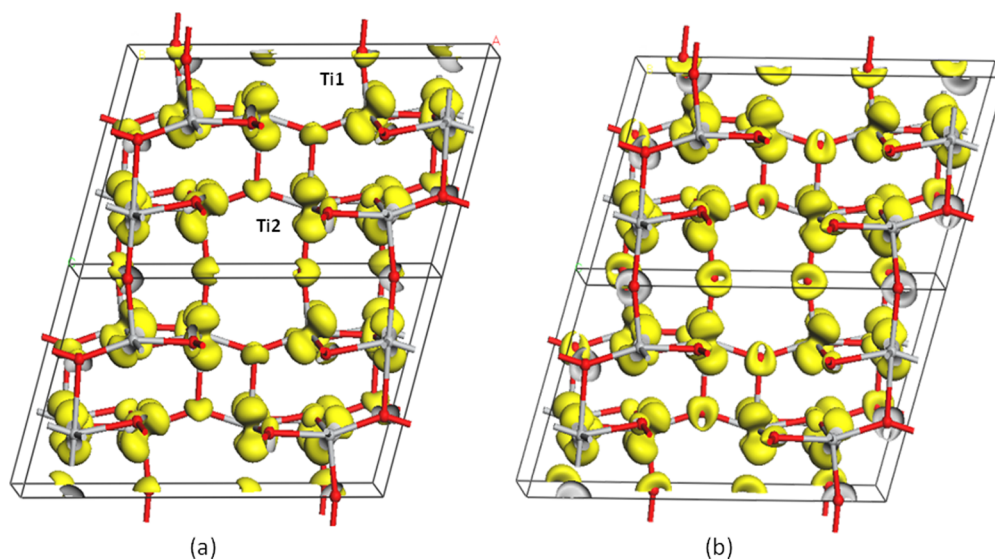
Figure 9. Fukui $f^+(r)$ function computed for $TiO_2(B)$ within the DFT+U framework at $U = 0$ (a) and $U = 7$ eV (b).

involved in the reduction process. As shown in Figure 9, the Fukui function computed at $U = 0$ clearly confirms that the first step of the electronic reduction should mainly involve the Ti1-d_{xy} and Ti2-d_{yz} orbitals, however, with an additional contribution of the Ti1-d_{yz} due to the distortion of the pyramid equatorial plane.

According to our analysis, the filling of these orbitals should then promote simultaneously the A1 and A2 sites for Li insertion, at least for the beginning of discharge.

This result is fully consistent with the Li-site relative energies listed in Supporting Information (SI-Figure 3) and previously reported by Morgan et al.[6] at small U values (<2 eV) for the $Li_{0.125}TiO_2$ composition, even though the Li composition and distribution considered for the site energy calculations ($x = 0.125$) are neither comparable to the electronic reduction assumed for the Fukui function (a fraction of electron) nor representative of the statistical A1/A2 distribution one should expect from the shape of the Fukui function. Interestingly, we note that for higher U values, the Fukui function shows only a slight increase of the Ti1-d_{yz} contribution. This suggests that the A2 site is even more activated at large U values than the A1 site.

Focusing now on the site energies at large U (see Supporting Information (SI-Figure 3)) we note that for $U > 4$ eV, A2 and 4g sites are favored over A1. As expected from the DFT+U formalism, the onset of U induces Ti−O bond elongations which primarily affect the titanyl-like Ti═O short bond of Ti1. Ti1 and Ti2 environments approach to each other which is fully consistent with the enlarged Ti1-d_{yz} contribution observed around Ti1 in the Fukui function at $U = 7$ eV compared to $U = 0$. The fact that the A1 site is so much disfavored in the calculations at large U and $x = 0.125$ is then linked to the Ti1(d_{xy})-orbital which is as less activated as the titanyl bond elongates. Furthermore, the bond elongation of the other Ti−O bonds of the structure, increases the electron density around the oxygen atoms lying in the (a,b) plane where the 4g sites are located (see Figure 9). This is also consistent with the stabilization of this site for large U values. Interestingly, we also note that when Li is initially in the C-site (i.e., 4g with $y = 0$) it becomes very unstable at large U values and spontaneously transforms into A2 site during the relaxation procedure. This

corroborates the nearly free energy barrier computed for the C → A2 reaction path[41] and clearly discards this site as a possible cationic site for Li insertion in $TiO_2(B)$. These results show that the A2 site is the most favored site for Li insertion at low lithium content, whatever the U value considered. It is favored over the other sites from the electronic point of view (Fukui function) and also from the ionic point of view (site energies). Whether the A1 or 4g site is second favored depends on the U values considered in the calculations. Given that the $TiO_2(B)$ experimental structure is better reproduced by our calculations at small U values (see Supporting Information, SI-Table 1), in particular, for the titanyl Ti═O short bond, we believe that rather smaller than larger U values should be used to investigate low Li-insertion content. As a consequence, only A1 and A2 should be considered in the first step of the discharge of $TiO_2(B)$ as possible sites for Li insertion, both of them being statistically distributed in the $TiO_2(B)$ structure. Consistently, both Ti1 and Ti2 ions should be simultaneously reduced upon reduction. This implicitly questions any attempt to rationalize the Li insertion mechanism in $TiO_2(B)$ by means of distinct Li-site relative energies, especially for Li compositions greater than $x = 0.125$ for which supercell calculations and statistical A1/A2/4g distributions must be considered.

Following, we will focus on the structural changes expected from our orbital analysis and Fukui function, in line of the experimental data reported above. The main question to address here is the evolution of the $TiO_2(B)$ unit cell parameters upon Li insertion, showing that a and b increase, while c remains constant up to 0.3 Li. In Figure 10, we have represented the local Ti1 and Ti2 environments as they appear in the $C2/m$ crystal structure of $TiO_2(B)$, where the Ti−O bonds mainly affected by Li insertion are illustrated by stiff (short bonds) and relaxed (long bonds) springs.

As nicely exemplified by Morgan et al.[6] with electron density maps computed at $x = 0.125$ for pure A1, A2, or C site occupation, Li insertion in the A1 site primarily affects the Ti1 electron density and, in particular, the d_{xy} orbital. According to the spatial expansion of this orbital, it interacts solely with the oxygen of the equatorial plane through antibonding interactions. Consequently, mainly the Ti1−O bonds oriented in the (a,b) plane should elongate, thus, logically echoing in the
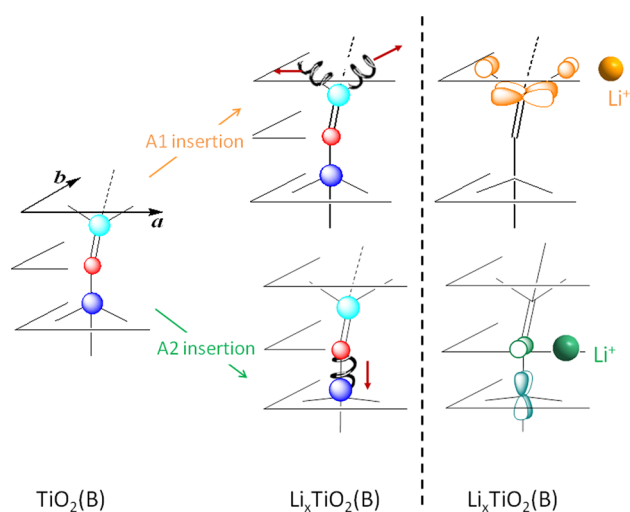
G

dx.doi.org/10.1021/jp507574e | J. Phys. Chem. C XXXX, XXX, XXX−XXX

Figure 10. Illustration of the structural changes induced in the local environment of Ti1O$_5$ and Ti2O$_6$ when Li$^+$ is inserted in the A1 and A2 sites and the associated electrons fill the antibonding Ti(d)−O(2p) orbitals.

increase of the a and b unit cell parameters (see Figure 2). The fact that this parameter increase is not echoed in the Ti−O and Ti−Ti shells (see Figure 5) is likely related to averaging effects: the filling of the A1 site at $x = 0.125$ increases the equatorial Ti−O bonds (increase of the Ti1−Ti2 along a and b) and simultaneously decreases some of the apical Ti−O bonds (decrease of the Ti1−Ti2 bonds along c). In average, this should render the local shells less sensitive to the slight structural modifications induced by Li insertion at low Li contents. Focusing on A2, Li insertion in this site primarily affects the Ti2 electron density and, in particular, the d_{yz} orbital. In this case, the Ti2−O bonds mainly affected by the electronic reduction are those running along the c-axis, namely, the apical Ti2−O bonds. In contrast to the A1 case, such bond elongation does not echo in the unit cell parameter response. In fact, as shown in Figure 10, the Ti2−O apical bond elongation triggers the displacement of the Ti2 ion along the c-axis, back to the equatorial plane of a more regular octahedron, which does not affect the c unit cell parameter.

This analysis thus suggests that the Li insertion into TiO$_2$(B) proceeds through the statistical occupation of A1 and A2 (at least up to $x = 0.125$), which is the only Li distribution allowing to rationalize the structural changes experimentally observed. As already mentioned above, a thorough analysis of higher Li compositions requires the calculations of statistical distributions together with large supercell calculations which is not the purpose of this work. We should note, however, that, due to the structural modifications occurring around Ti1 and Ti2 from $x = 0$ and $x = 0.125$, further Li insertion may involve other d-orbitals, especially for the Ti2 ion, which is shown to adopt a more octahedral-like environment from $x = 0.125$.

We show here that the knowledge of the Ti1 and Ti2 local environments in TiO$_2$(B) is crucial for identifying which of the local metallic orbitals are involved in the electrochemical properties of this system. These orbitals provide quantification axes for the electronic reduction, which are further used to selectively spot which of the Li$^+$-cationic sites are promoted upon lithiation and how the crystal structure responds to this electrochemical Li insertion. We believe such analysis provides a robust link between the local structure of the redox active

centers and the electrochemical and structural response of the system.

■ CONCLUSIONS

In this study, we developed and carried out XRD and XAS operando measurements coupled to DFT calculations and local chemical bond analyses to investigate lithium insertion and deinsertion in TiO$_2$(B) phase. Our results show that TiO$_2$(B) features a completely monophasic insertion mechanism associated with the statistical occupation of sites A1 and A2. A reversible anisotropic lattice expansion accompanied by a gradual reversible reduction of Ti^{IV} upon lithium insertion is also observed. This observation is fully rationalized using an orbital approach which selectively spots Li-site preferences and furthermore explains their respective impact on the Ti local environments. Additionally, the existence of an outer oxygen shell at 2.4 Å undergoing strong elongation once lithium insertion exceeds 0.4 Li is proposed on the basis of the analysis of the EXAFS data, while the other next neighbors undergo a rather small and steady expansion. This result has to be taken with caution since it is based on local pyramidal-like environment for titanium, which might not be as consistent as for low Li contents. The insights gained in this work will contribute to the understanding of the distinct lithium electrochemical cycling properties of this promising insertion material.

■ ASSOCIATED CONTENT

ⓢ Supporting Information
XAFS Fourier transform and real space contribution for different oxygen repartition model, as well as relative Li-site energies for A1, A2, and 4g as a function of U. This material is available free of charge via the Internet at http://pubs.acs.org.

■ AUTHOR INFORMATION

Corresponding Authors
*E-mail: marcus.fehse@univ-montp2.fr.
*E-mail: lorenzo.stievano@univ-montp2.fr. Phone: +33 (0)4 67 14 33 46. Fax: +33 (0)4 67 14 33 04.
Notes
The authors declare no competing financial interest.

■ ACKNOWLEDGMENTS

■ REFERENCES

(1) Nuspl, G.; Yoshizawa, K.; Yamabe, T. Lithium intercalation in TiO$_2$ modifications. *J. Mater. Chem.* **1997**, *7*, 2529−2536.
(2) Brohan, L.; Marchand, R. Properties physiques des bronzes M$_x$TiO$_2$ (B). *Solid State Ionics* **1983**, *910*, 419−424.
(3) Zachau-Christiansen, B.; West, K.; Jacobsen, T. Lithium insertion in different TiO$_2$ modifications. *Solid State Ionics* **1988**, *30*, 1176−1182.

(4) Armstrong, A. R.; Armstrong, G.; Canales, J.; Garca, R.; Bruce, P. G. Lithium-ion intercalation into $TiO_2(B)$ nanowires. *Adv. Mater.* **2005**, *17*, 862−865.

(5) Zukalova, M.; Kalbac, M.; Kavan, L.; Exnar, I.; Graetzel, M. Pseudocapacitive lithium storage in $TiO_2(B)$. *Chem. Mater.* **2005**, *17*, 1248−1255.

(6) Morgan, B. J.; Madden, P. a. Lithium intercalation into $TiO_2(B)$: A comparison of LDA, GGA, and GGA+U density functional calculations. *Phys. Rev. B* **2012**, *86*, 035147.

(7) Liu, S.; Jia, H.; Han, L.; Wang, J.; Gao, P.; Xu, D.; Yang, J.; Che, S. Nanosheet-constructed porous $TiO_2(B)$ for advanced lithium Ion batteries. *Adv. Mater.* **2012**, *24*, 3201−3204.

(8) Fehse, M.; Fischer, F.; Tessier, C.; Stievano, L.; Monconduit, L. Tailoring of phase composition and morphology of TiO_2-based electrode materials for lithium-ion batteries. *J. Power Sources* **2013**, *231*, 23−28.

(9) Aravindan, V.; Shubha, N.; Cheah, Y. L.; Prasanth, R.; Chuiling, W.; Prabhakar, R. R.; Madhavi, S. Extraordinary long-term cycleability of TiO_2-B nanorods as anodes in full-cell assembly with electrospun PVdF-HFP membranes. *J. Mater. Chem. A* **2013**, *1*, 308.

(10) Armstrong, A. R.; Armstrong, G.; Canales, J.; Bruce, P. G. TiO_2-B nanowires. *Angew. Chem., Int. Ed.* **2004**, *43*, 2286−8.

(11) Wang, B.; Chen, Q.; Hu, J.; Li, H.; Hu, Y.; Peng, L.-M. Synthesis and characterization of large scale potassium titanate nanowires with good Li-intercalation performance. *Chem. Phys. Lett.* **2005**, *406*, 95−100.

(12) Li, J.; Wan, W.; Zhou, H.; Li, J.; Xu, D. Hydrothermal synthesis of $TiO_2(B)$ nanowires with ultrahigh surface area and their fast charging and discharging properties in Li-ion batteries. *Chem. Commun.* **2011**, *47*, 3439−41.

(13) Arrouvel, C.; Parker, S. C.; Islam, M. S. Lithium insertion and transport in the $TiO_2(B)$ anode material: A computational study. *Chem. Mater.* **2009**, *21*, 4778−4783.

(14) Armstrong, A. R.; Arrouvel, C.; Gentili, V.; Parker, S. C.; Islam, M. S.; Bruce, P. G. Lithium coordination sites in $Li_xTiO_2(B)$: A structural and computational study. *Chem. Mater.* **2010**, *22*, 6426−6432.

(15) Dylla, A. G.; Xiao, P.; Henkelman, G.; Stevenson, K. J. Morphological dependence of lithium insertion in nanocrystalline $TiO_2(B)$ nanoparticles and nanosheets. *J. Phys. Chem. Lett.* **2012**, *2*, 2015−2019.

(16) Okumura, T.; Fukutsuka, T.; Yanagihara, A.; Orikasa, Y.; Arai, H.; Ogumi, Z.; Uchimoto, Y. Electronic and local structural changes with lithium-ion insertion in TiO_2-B: X-ray absorption spectroscopy study. *J. Mater. Chem.* **2011**, *21*, 15369−15377.

(17) Okumura, T.; Fukutsuka, T.; Yanagihara, A.; Orikasa, Y.; Arai, H.; Ogumi, Z.; Uchimoto, Y. Nanosized effect on electronic/local structures and specific lithium-ion insertion property in $TiO_2(B)$ nanowires analyzed by X-ray absorption spectroscopy. *Chem. Mater.* **2011**, *23*, 3636−3644.

(18) Dalton, A.; Belak, A.; Ven, A. V. D. Thermodynamics of lithium in $TiO_2(B)$ from first principles. *Chem. Mater.* **2012**, *24*, 1568−1574.

(19) Koudriachova, M. V. Role of the surface in Li insertion into nanowires of $TiO_2(B)$. *Surf. Interface Anal.* **2010**, *42*, 1330−1332.

(20) Hoshina, K.; Harada, Y.; Inagaki, H.; Takami, N. Character-ization of lithium storage in $TiO_2(B)$ by 6Li-NMR and X-ray diffraction analysis. *J. Electrochem. Soc.* **2014**, *161*, A348−A354.

(21) Fehse, M.; Fischer, F.; Tessier, C.; Stievano, L.; Monconduit, L. Study of the insertion mechanism of lithium into anatase by operando X-ray diffraction and absorption spectroscopy. *Solid State Ionics* **2014**, http://dx.doi.org/10.1016/j.ssi.2014.09.018.

(22) Leriche, J. B.; Hamelet, S.; Shu, J.; Morcrette, M.; Masquelier, C.; Ouvrard, G.; Zerrouki, M.; Soudan, P.; Belin, S.; et al. An electrochemical cell for operando study of lithium batteries using synchrotron radiation. *J. Electrochem. Soc.* **2010**, *157*, A606−A610.

(23) Kraus, W.; Nolzeb, G. POWDER CELL a program for the representation and manipulation of crystal structures and calculation of the resulting X-ray powder patterns. *J. Appl. Crystallogr.* **1996**, *29*, 301−303.

(24) Rodrguez-Carvajal, J. Recent advances in magnetic structure determination by neutron powder diffraction. *Phys. B (Amsterdam, Neth.)* **1993**, *193*, 55−69.

(25) Ben Yahia, M.; Lemoigno, F.; Beuvier, T.; Filhol, J.-S.; Richard-Plouet, M.; Brohan, L.; Doublet, M.-L. Updated references for the structural, electronic, and vibrational properties of $TiO_2(B)$ bulk using first-principles density functional theory calculations. *J. Chem. Phys.* **2009**, *130*, 204501−11.

(26) Rehr, J. J.; Mustre de Leon, J.; Zabinsky, S. I.; Albers, R. C. Theoretical X-ray absorption fine structure standards. *J. Am. Chem. Soc.* **1991**, *113*, 5135−5140.

(27) Anisimov, V. I.; Zaanen, J.; Andersen, O. K. Band theory and Mott insulators: Hubbard U instead of Stoner I. *Phys. Rev. B* **1991**, *44*, 943−954.

(28) Dudarev, S. L.; Savrasov, S. Y.; Humphreys, C. J.; Sutton, A. P. Electron-energy-loss spectra and the structural stability of nickel oxide: An LSDA+U study. *Phys. Rev. B* **1998**, *57*, 1505−1509.

(29) Kresse, G.; Hafner, J. Ab initio molecular dynamics for liquid metals. *Phys. Rev. B* **1993**, *47*, 558−561.

(30) Kresse, G.; Furthmüller, J. Efficiency of ab-initio total energy calculations for metals and semiconductors using a plane-wave basis set. *Comput. Mater. Sci.* **1996**, *6*, 15−50.

(31) Perdew, J.; Burke, K.; Ernzerhof, M. Generalized gradient approximation made simple. *Phys. Rev. Lett.* **1996**, *77*, 3865−3868.

(32) Kresse, G.; Joubert, D. From ultrasoft pseudopotentials to the projector augmented-wave method. *Phys. Rev. B* **1999**, *59*, 1758−1775.

(33) Parr, R. G.; Yang, W. *Density-functional theory of atoms and molecules*; Oxford University Press: New York, 1989.

(34) Fehse, M.; Cavaliere, S.; Lippens, P. E.; Savych, I.; Iadecola, A.; Monconduit, L.; Jones, D. J.; Rozière, J.; Fischer, F.; et al. Nb-doped TiO_2 nanofibers for lithium ion batteries. *J. Phys. Chem. C* **2013**, *117*, 13827−13835.

(35) Lafont, U.; Carta, D.; Mountjoy, G.; Chadwick, A. V.; Kelder, E. M. In situ structural changes upon electrochemical lithium insertion in nanosized anatase TiO_2. *J. Phys. Chem. C* **2010**, *114*, 1372−1378.

(36) Luca, V.; Hanley, T.; Roberts, N.; Howe, R. NMR and X-ray absorption study of lithium intercalation in micro-and nanocrystalline anatase. *Chem. Mater.* **1999**, *11*, 2089−2102.

(37) Parlebas, J.; Khan, M.; Uozumi, T.; Okada, K.; Kotani, A. Theory of many-body effects in valence, core-level and isochromat spectroscopies along the 3d transition metal series of oxides. *J. Electron Spectrosc. Relat. Phenom.* **1995**, *71*, 117−139.

(38) Brutti, S.; Gentili, V.; Reale, P.; Carbone, L.; Panero, S. Mitigation of the irreversible capacity and electrolyte decomposition in a $LiNi_{0.5}Mn_{1.5}O_4$/nano-TiO_2 Li-ion battery. *J. Power Sources* **2011**, *196*, 9792−9799.

(39) Beuvier, T.; Richard-Plouet, M.; Mancini-Le Granvalet, M.; Brousse, T.; Crosnier, O.; Brohan, L. $TiO_2(B)$ nanoribbons as negative electrode material for lithium ion batteries with high rate performance. *Inorg. Chem.* **2010**, *49*, 8457−64.

(40) Armstrong, A. R.; Armstrong, G.; Canales, J.; Bruce, P. G. $TiO_2(B)$ nanowires as negative electrodes for rechargeable lithium batteries. *J. Power Sources* **2005**, *146*, 501−506.

(41) Panduwinata, D.; Gale, J. D. A first principles investigation of lithium intercalation in TiO_2-B. *J. Mater. Chem.* **2009**, *19*, 3931.

I

dx.doi.org/10.1021/jp507574e | *J. Phys. Chem. C* XXXX, XXX, XXX−XXX